RSC Advances

PAPER

View Article Online
View Journal | View Issue

Cite this: *RSC Adv.*, 2025, **15**, 26383

Next-generation optical sensing: mesoporous hollow-shell nanostructured one-dimensional photonic crystal sensors for sCD40L detection in acute coronary syndrome

Xiaoqi Li,†[a] Zhiyu Zhang,†[a] Liyuan Wang,†[c] Taotao Liu,[d] Heng Zhu,[ae] Lei Rong,[a] Yun Du,[a] Changpeng Zhai,[f] Shaoshen Wang,*[ag] Jie Tan*[ab] and Jing Huang *[a]

Acute coronary syndrome (ACS) refers to a group of clinical symptoms resulting from acute ischemia of the coronary arteries. Studies have shown that the level of soluble CD40 ligand (sCD40L) is significantly elevated in patients with ACS, making it a novel target for cardiovascular disease treatment. In response, this study proposes an optical sensor based on a modified single-crystal silicon substrate. The sensor utilizes PEG/TiO_2 as the sensing element and sCD40L@SL-mTiO_2 nanoparticles as the recognition molecules, enabling highly specific detection of sCD40L while incorporating a self-cleaning capability. Upon exposure to ultraviolet light, the sensor not only detects the concentration of sCD40L with high sensitivity and accuracy, but also degrades bacteria and decomposes organic matter *via* photochemical reactions, thereby enabling an effective self-cleaning function. The research findings indicate that this one-dimensional (1D) photonic crystal sensor is capable of rapidly and accurately conducting qualitative detection of sCD40L, demonstrating great potential for efficient analysis of biological samples. The application of this sensor not only provides a novel technological pathway for early cardiovascular disease diagnosis but also offers theoretical support for related drug development and clinical diagnostics.

Received 8th May 2025
Accepted 11th July 2025

DOI: 10.1039/d5ra03238e

rsc.li/rsc-advances

1 Introduction

Acute Coronary Syndrome (ACS) is a severe manifestation of coronary artery disease (CAD). Its clinical manifestations vary widely, with the primary symptoms including chest pain, chest tightness, and a burning sensation in the chest. In severe cases, ACS may lead to cardiogenic shock, acute heart failure, or sudden cardiac arrest. These conditions may occur with or without changes in a 12-lead electrocardiogram (ECG) and may or may not be accompanied by an acute elevation in troponin levels.[1,2] Epidemiological studies have shown that coronary artery disease (CAD) is the leading cause of disease-related mortality worldwide. In the United States alone, approximately one million individuals experience acute myocardial infarction (AMI) annually. Notably, AMI-related fatalities account for over half of all deaths attributed to coronary heart disease.[3,4] Early prevention and treatment of ACS are crucial for improving patient survival rates. However, some elderly patients may present with atypical symptoms, leading to misdiagnosis or missed diagnosis.[5] The detection of relevant biomarkers plays a crucial role in the early screening, assessment, and monitoring of ACS patients, significantly contributing to improving their survival rates.

sCD40L is a type II transmembrane protein classified within the tumor necrosis factor (TNF) superfamily. It is primarily expressed in trimeric form on the surface of activated T cells, platelets, and various other immune cells.[6,7] Acting as a pivotal molecule at the intersection of inflammation and immunity, sCD40L binds to CD40, thereby triggering inflammatory responses, modulating immune cell activity, and promoting cytokine secretion.[8,9] Moreover, elevated levels of sCD40L can be detected in the serum of patients with ACS. By promoting the expression of matrix metalloproteinases (MMPs), sCD40L compromises the integrity of the fibrous cap, making plaques more prone to rupture.[10,11] Research has shown that sCD40L

[a]*Department of Cardiology, The Second Affiliated Hospital of Chongqing Medical University, Chongqing, China. E-mail: 2024140223@stu.cqmu.edu.cn; 2023440001@stu.cqmu.edu.cn; huangjing@cqmu.edu.cn*

[b]*Department of Cardiology, The People's Hospital of Kaizhou District, Chongqing, China*

[c]*National Clinical Research Center for Cancer, Tianjin Medical University Cancer Institute and Hospital, Tianjin, China*

[d]*Department of Neurogastroenterology & Pelvic Floor Surgery Disease, Xi'an International Medical Center Hospital, Xi'an, China*

[e]*Department of Cardiology, The Second Affiliated Hospital of Chengdu Medical College, Sichuan, China*

[f]*Department of Cardiology, Affiliated Hospital of Hebei Engineering University, Handan, China*

[g]*Department of Cardiology, The Affiliated Hospital of Xuzhou Medical University, Jiangsu, China*

† These authors contributed equally to this work and share first authorship.

levels can predict both short-term and long-term outcomes in ACS patients, with its prognostic value being particularly significant in high-risk individuals.[10] Therefore, serum sCD40L is a potential biomarker with significant implications for the diagnosis and prevention of ACS. The development of sCD40L detection devices represents a milestone in ACS diagnostics and the advancement of related therapeutic drugs.

In recent years, research on sensors for tumor marker detection has advanced significantly, driven by their ultra-sensitive recognition capabilities and broad adaptability.[12] As a novel liquid biopsy technology, this approach offers quantitative or semi-quantitative insights into specific analytes by coupling biological recognition elements (BRE) with sensing components.[13] Compared with traditional diagnostic methods, sensors possess key advantages such as portability, specificity, high sensitivity, and minimal sample preparation.[14] It was also found that the localized surface plasmon resonance (LSPR) effect can enhance the sensor's response to environmental changes, thereby improving its detection sensitivity.[15,16] Li *et al.* found that based on the SPR effect, the graphene absorber demonstrated four ideal absorption peaks from 7 to 12 THz, with an average absorption efficiency of 99.61%.[17] The integration of nanotechnology with sensing technology has markedly improved the analytical performance of sensors by enhancing their sensitivity and signal amplification. This advancement facilitates the application of such sensors in ACS detection, advancing early diagnostic capabilities to a new level.

In 1D photonic crystal sensors, chemical reactions typically occur at the interface between the sensor surface and the surrounding solution. During these reactions, analytes, intermediates, and polymeric byproducts often accumulate and adsorb to the sensor surface, significantly affecting its lifespan and sensitivity. Effectively regenerating and reusing photonic crystal sensors remains a major challenge in sensor development, posing a critical hurdle for researchers in the field. Therefore, selecting a mild and suitable method to remove residues and contaminants *via* a self-cleaning process is of considerable research interest. Studies have demonstrated that composite materials incorporating the photocatalyst TiO_2, which enables visible-light-driven photocatalytic degradation, can impart self-cleaning capabilities to sensors.[18] Zhu *et al.* explored a bioelectrochemical sensor based on carbon-doped TiO_2 nanotubes. A TiO_2 nanotube array was fabricated *via* carbon doping and employed for the detection of serotonin and uric acid. After detection, the sensor was exposed to ultraviolet light, and the results confirmed its excellent self-cleaning capabilities, underscoring its potential for reuse and long-term application.[19] This finding further demonstrates the remarkably strong self-cleaning capability of TiO_2, laying a solid foundation for its application as a self-cleaning material.

With advancements in science and technology, an increasing number of sensors with wide detection ranges and high sensitivity have been developed. However, the excessive use of materials has resulted in significant waste accumulation and environmental pollution. Additionally, when applying 1D photonic crystals, bacterial proliferation can pose a serious threat to human health, underscoring the necessity of innovative and sustainable solutions.[20] Therefore, during sample detection, sensor substrates must not only exhibit self-cleaning properties but also be both environmentally friendly and antibacterial. Due to its high efficiency and broad-spectrum antibacterial activity, TiO_2 has emerged as a key focus in the research and development of antibacterial materials.[21] Zhao *et al.* conducted antibacterial experiments on a porous TiO_2 coating doped with Si and Ag. The results confirmed that the coating exhibited notable antibacterial properties, highlighting its potential for antimicrobial applications.[22] This further validates the antibacterial properties of TiO_2. A literature review revealed that no previous studies have reported the detection of sCD40L using PEG/TiO_2 as the sensing element and R@SL-mTiO_2 as the recognition element.

In this study, we incorporated two materials with significantly different refractive indices—PEG and TiO_2—into the sensing element of a 1D photonic crystal sensor. Utilizing the principle that the binding of the recognition element sCD40L@SL-mTiO_2 to sCD40L molecules in the serum of ACS patients alters the thickness of the sensor's layered structure, we induced a shift in the photonic bandgap, which in turn caused a visible change in the sensor's surface color. This enabled the visual detection of sCD40L. Relevant experiments have also shown that the 1D photonic crystal visual sensor based on PEG/TiO_2 not only retains the sensitivity of the photonic crystal but also inherits the photocatalytic and antibacterial properties of TiO_2. This dual functionality allows for rapid disease diagnosis while simultaneously inhibiting the growth of pathogenic microorganisms in the tested samples, degrading residual waste, and preventing environmental pollution.

2 Materials and methods

2.1 Materials

E. coli BL21 was preserved by the Second Affiliated Hospital of Chongqing Medical University. LB medium and PBS components were purchased from Hopebio (Haibo Bio, China). Soluble CD40 ligand was obtained from Houpu Biotech (Zhenjiang, Jiangsu, China). Tetra-*n*-butyl titanate and rhodamine B were purchased from Shanghai Maklin Biochemical Co., Ltd Anhydrous ethanol (analytical grade), acetone, tetrahydrofuran, acetic acid, Pluronic F127, 1,3,5-trimethylbenzene, NaOH, glacial acetic acid (analytical grade), concentrated sulfuric acid (98%, analytical grade), and 30% hydrogen peroxide (analytical grade) were purchased from China National Pharmaceutical Group Corporation Chemical Reagents Co., Ltd Branched polyethylenimine (PEG, ≥99%) was purchased from Sigma (St. Louis, USA). Silica was obtained from Xianfeng Nano Company.

2.2 Preparation and characterization of sensing device

2.2.1 Surface modification of single-crystal silicon. Silicon wafers (1.5 × 1.5 cm) were cleaned by ultrasonic treatment in acetone and ethanol (20 min each), then immersed in piranha solution ($H_2SO_4 : H_2O_2 = 3 : 1$) for 2 hours. Finally, they were

rinsed with deionized water (ultrasonicated 30 min) and dried under nitrogen.

2.2.2 Preparation of the sensing element PEG/TiO_2. Dissolve PEG in distilled water and set aside. Mix 4 mL tetrabutyl titanate with 2 mL glacial acetic acid, then add to 42 mL anhydrous ethanol. Stir at room temperature for 4 hours to obtain TiO_2 gel for later use.

2.2.3 Preparation of the recognition element sCD40L@SL-mTiO_2. Pluronic F127, acetic acid, and HCl (3.2 mL) were added to THF (30 mL), followed by dropwise addition of titanium butoxide. After stirring for 10 min, the mixture was heated at 45 °C for 24 h to form the F127/TiO_2 gel. The gel was mixed with 1,3,5-trimethylbenzene (3 mL), stirred, then dispersed in anhydrous ethanol (10 mL). Ethanol solution (2 mL) containing monodisperse SiO_2 (1.0 g) was added. The mixture was heated at 100 °C for 6 h, then centrifuged, washed, and dried. After annealing at 350 °C under N_2 for 3 h, the F127 template was removed to yield SiO_2@SL-mTiO_2. Etching with NaOH at 80 °C produced hollow SL-mTiO_2, which was freeze-dried for preservation.

Prepared nanoparticles were mixed with sCD40L antibody solution, ultrasonicated for 1 h, then centrifuged to remove unbound antibodies. The resulting sCD40L@SL-mTiO_2 nanomedicine was resuspended for further use.

2.2.4 Fabrication of the 1D photonic crystal sensor. The previously prepared TiO_2 gel, sCD40L@SL-mTiO_2 nanomedicine, and PEG solution were alternately deposited onto a single-crystal silicon substrate *via* spin coating. In this experiment, the initial spin speed was set to 3500 rpm. After adding 500 μL of TiO_2 solution, spin coating was carried out at specific secondary spin speeds and varied coating times. The spin coating time was 60 seconds, followed by heating in an 80 °C oven for 10 minutes. Subsequently, 250 μL of sCD40L@SL-mTiO_2 was added, and high-speed spin coating was performed for 60 seconds, followed by another 10 minutes of heating in the oven. Under the same conditions, 500 μL of PEG solution was added, followed by high-speed spin coating for 60 seconds, and then heating in an 80 °C oven for 10 minutes. The total number of layers of the film was 3 N, with the first layer being TiO_2 and the final layer being PEG. The film was then stored at 4 °C for future use.

2.3 Detection of sCD40L using sensing devices

2.3.1 Study on the response performance of sensor. Detect the response changes of the optical sensor under different concentrations of sCD40L to evaluate the sensor's sensitivity to sCD40L concentration. Prepare sCD40L solutions of different concentrations using PBS, with concentration ranges of (0 ng mL^{-1}, 5 ng mL^{-1}, 10 ng mL^{-1}, 50 ng mL^{-1}, 100 ng mL^{-1}). At the same time, to exclude the impact of common interfering substances in serum on the detection results, as well as to investigate the specificity of the sensor, ascorbic acid (AA), uric acid (UA), and bovine serum albumin (BSA) at the same concentration (100 ng mL^{-1}) were further selected for the study.

2.3.2 Clinical application study of sensor for sCD40L detection. Centrifuge blood samples from patients with ACS and normal patients (both obtained from Kaizhou District People's Hospital, Chongqing) at 3000 rpm for 5 minutes. Collect the supernatant, dilute it 10-fold, and store it for later use. Use a Human sCD40L ELISA kit to verify the sCD40L levels in the serum of patients with acute coronary syndrome.

Drop the test samples onto the surface of PEG/TiO_2@-sCD40L@SL-mTiO_2. After 1 hour, collect the samples from the sensor surface and gently rinse the sensor with deionized water. Then, remeasure the reflection spectrum of the photonic crystal using a fiber optic spectrometer.

2.4 Detection of organic decomposition performance of sensing element

Rhodamine B, as an organic dye, is widely used in experimental science. In this study, rhodamine B was used as a model compound in the decomposition experiment of PEG/TiO_2@-sCD40L@SL-mTiO_2. Standard rhodamine B solutions were prepared at concentrations of 0.25 mg mL^{-1}, 0.5 mg mL^{-1}, 1 mg mL^{-1}, 2 mg mL^{-1}, and 4 mg mL^{-1}. The absorbance of the solutions was measured using a UV spectrophotometer in the wavelength range of 300–750 nm.

Rhodamine B was selected as the target compound, with control and experimental groups established to evaluate its organic decomposition performance. Samples were taken at regular intervals, and the OD value of the sample solution at 550 nm was measured using a UV spectrophotometer. A decomposition curve was then plotted.

2.5 Antibacterial performance evaluation of sensing element

Frozen *E. coli* BL21 was retrieved from −80 °C and quickly thawed. Using an inoculation loop, the bacteria were streaked onto LB agar and incubated overnight at 37 °C. Once single colonies appeared, one colony was picked and inoculated into liquid LB medium, followed by incubation at 200 rpm and 37 °C.

A standard *E. coli* suspension was prepared and adjusted to the desired concentration. A PBS-treated group served as the blank control. The prepared sensors and single-crystal silicon wafers were UV-sterilized prior to use. For the control group, 50 μL of PBS was added to the surface of the Si wafer. Then, 50 μL of the bacterial suspension was added to both the Si wafers and the sensor surfaces.

Samples were incubated at 37 °C, and bacterial suspensions were collected from wafer surfaces at 12 h and 24 h. The absorbance at 600 nm was measured using a microplate reader. The collected suspensions were serially diluted and inoculated onto agar plates to observe bacterial growth. Additionally, a live/dead bacterial staining kit was used to evaluate bacterial viability.

3 Results and discussion

3.1 Characterization of PEG/TiO_2@sCD40L@SL-mTiO_2

3.1.1 Characterization of the sensor device using scanning electron microscopy (SEM) and transmission electron microscope (TEM). SEM can be used to characterize the distribution

and morphology of the sensing and recognition elements on the surface of single-crystal silicon. In this experiment, modified single-crystal silicon and the prepared photonic crystal sensor were sampled for SEM analysis. The planar SEM results of the modified single-crystal Si and PEG/TiO_2@sCD40L@SL-mTiO_2 are shown in Fig. 1D. The surface of the single-crystal Si is smooth and free of obvious particles. In contrast, the sensor surface is covered with numerous spherical nanoparticles, which are uniform in size and evenly distributed. The cross-sectional SEM results of the modified single-crystal Si and PEG/TiO_2@sCD40L@SL-mTiO_2 are shown in Fig. 1E. Since the prepared nanocapsules were not added to the surface of the single-crystal Si, its SEM results show fewer layered structures in the cross-section. However, after the introduction of nanocapsules, the cross-sectional SEM images of the crystal sensor group exhibit a distinct multilayer structure. Compared to single-crystal silicon, the multilayer structure of the crystal sensor group indicates that the nanocapsules are more evenly attached and distributed on the surface of the silicon. The TEM images distinctly reveal well-defined hollow nanoparticles with a uniform and spherical morphology. The pronounced contrast between the darker outer shell and the lighter interior region provides clear evidence of their hollow structure. Furthermore, the nanoparticles are monodispersed and show minimal aggregation, indicating excellent colloidal stability.

Nanomaterials are commonly used to enhance biosensors because of their excellent conductivity, biocompatibility, and the ability to facilitate the immobilization of antibodies and signal amplification. Nanoparticles can combine light absorption bands and in-body diffraction resonance through surface plasmon resonance (SPR), which alters the optical properties of photonic crystals.[23–25] In this study, SL-mTiO_2 was incorporated as a carrier for the Anti-sCD40L Antibody to enhance its loading efficiency. Meanwhile, due to its high specific surface area and unique photoelectric properties, SL-mTiO_2 can improve the sensor's detection sensitivity for sCD40L. By integrating

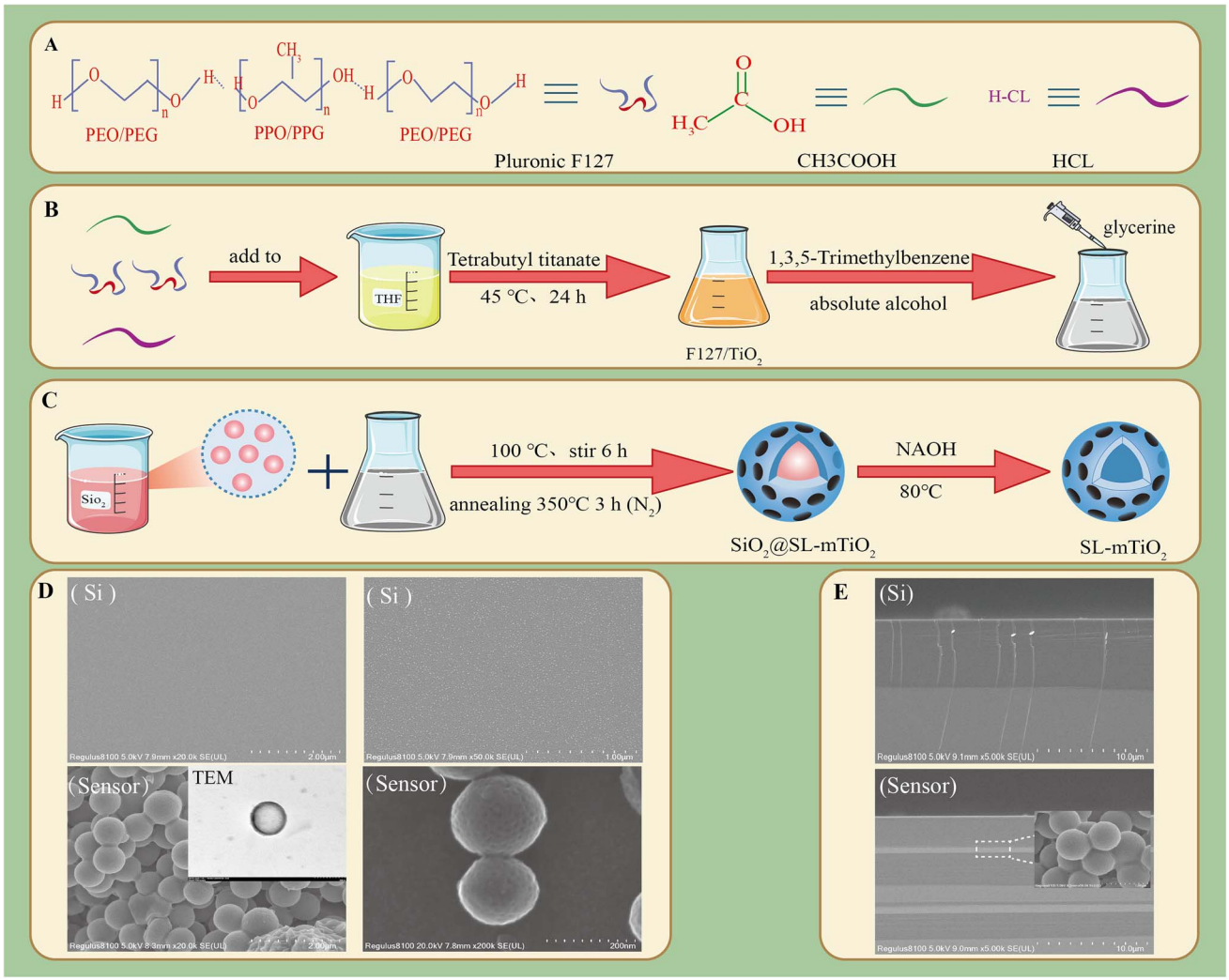

Fig. 1 Scanning Electron Microscopy (SEM) and Transmission Electron Microscopy (TEM) images of PEG/TiO_2@sCD40L@SL-mTiO_2 and related materials. (A–C) Schematic illustration of the preparation process of SL-mTiO_2 nanoparticles. (D) SEM and TEM images of modified single-crystal silicon (Si) and PEG/TiO_2@sCD40L@SL-mTiO_2. (E) Cross-sectional SEM images of modified single-crystal silicon and PEG/TiO_2@sCD40L@SL-mTiO_2.

nanomaterials with a photonic crystal sensor, the Anti-sCD40L Antibody specifically recognizes and captures sCD40L. This interaction causes changes in the structure and volume of the entire nanoparticle layer, enabling the rapid detection of sCD40L.

3.1.2 Optical characterization of the sensing device. A photonic crystal refers to a structure formed by the periodic spatial arrangement of two or more materials with different refractive indices.[26] 1D photonic crystals are typically fabricated using the spin-coating method, which involves adjusting the rotational speed of the spin coater to control the thickness and arrangement of the thin film on the crystal surface.[27] When the spin coater's rotational speed is set to 3500 rpm, a high-speed spin-coating duration of 20 s is followed by low-speed spin-coating durations of 5 s, 10 s, 15 s, and 20 s. During this process, PEG solution and TiO_2 gel are alternately spin-coated onto a silicon wafer. This process results in the fabrication of PEG/TiO_2 1D photonic crystals with different photonic bandgaps (Fig. 2A). The results show (Fig. 2B and C) that PEG/TiO_2 appears purple at 420 nm, blue at 480 nm, green at 550 nm, and yellow at 570 nm. This phenomenon is primarily due to the periodic variations in the refractive index of photonic crystals, which provide localized optical modes. These variations result in Bragg scattering effects, which cause the reflection spectrum to display characteristic reflection peaks. This indicates that photons with frequencies within the bandgap are prohibited from propagating within the photonic crystal and are thus completely reflected.[28]

During the preparation process, we further observed that the spin-coating speed has a significant impact on the reflection spectrum of PEG/TiO_2 (Fig. 2D). By setting the spin coater's rotational speeds to 1500 rpm, 2500 rpm, 3500 rpm, 4500 rpm, and 5500 rpm, PEG/TiO_2 photonic crystals with different photonic bandgaps were fabricated. The results show that as the spin-coating speed increases, the reflection spectrum of PEG/TiO_2 shifts noticeably to the right. By adjusting the rotational speed of the spin coater, the thickness of the thin film can be indirectly changed, which in turn causes a shift in the photonic bandgap. This phenomenon also conforms to Bragg's law, which states that, at a fixed incident angle, a reduction in the film thickness leads to a corresponding decrease in the reflected wavelength.[29,30] Therefore, by adjusting the spin-coating speed to control the bandgap position of the photonic crystal, photonic crystals with different colors can be fabricated.

In this study, a periodic structure in the 1D direction is formed by layer-by-layer stacking of two different dielectric

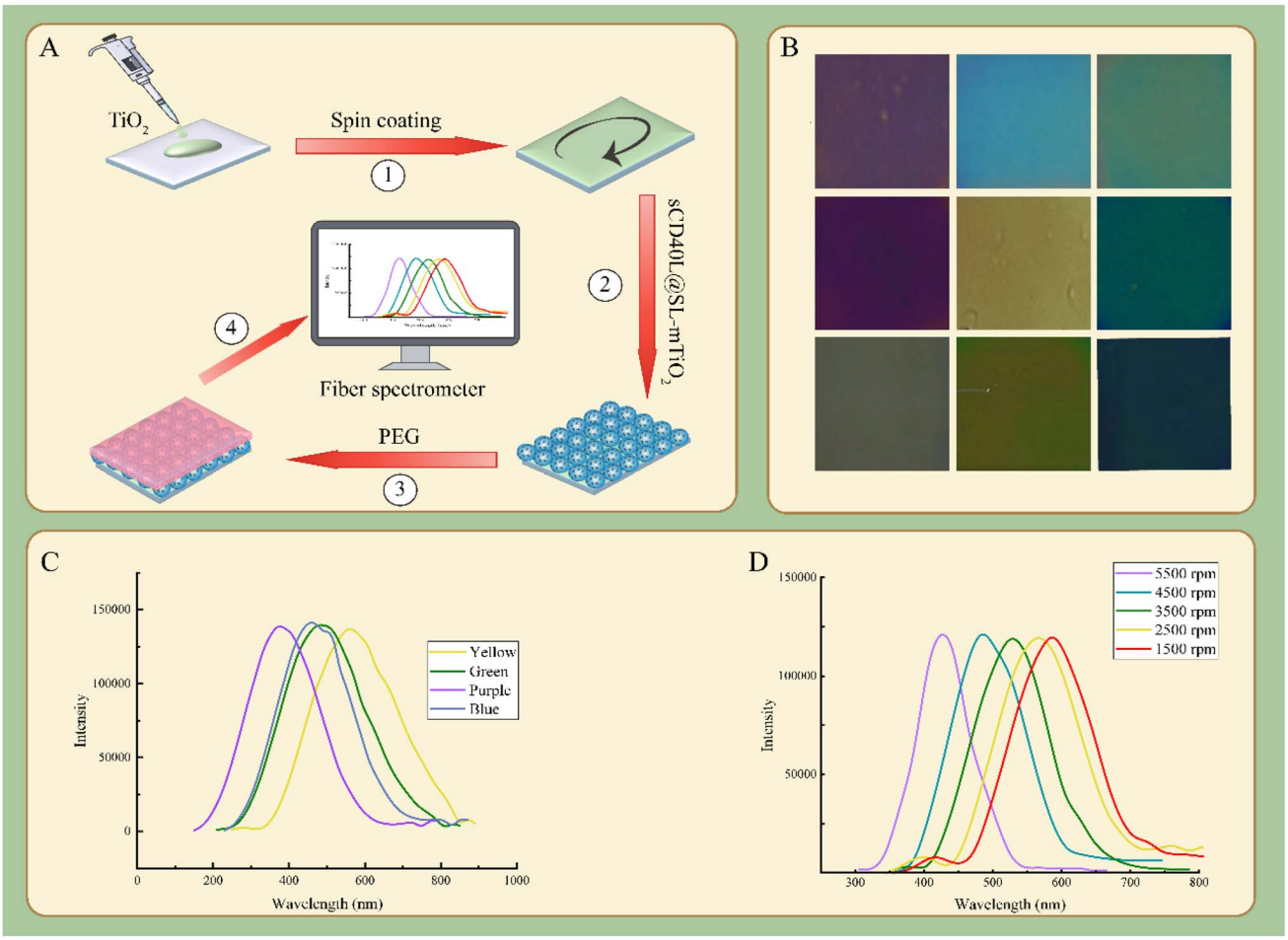

Fig. 2 Optical characterization of PEG/TiO_2. (A) Preparation process of PEG/TiO_2. (B) The fabricated PEG/TiO_2 photonic crystals of different colors. (C and D) Reflection spectra of photonic crystals fabricated at different rotational speeds.

materials, PEG and TiO_2, which can also be referred to as a Bragg reflector. This type of reflector features a simple structure, high reflectivity, and predictable optical properties.[31] In this study, PEG/TiO_2 is used as the sensing element and sCD40L@SL-mTiO_2 as the recognition element. The application of this system for sCD40L detection, as well as its self-cleaning and antibacterial effects during disease detection, is investigated. The aim is to provide new approaches and methods for the rapid detection of sCD40L.

3.2 Detection of sCD40L by the sensing device

To evaluate the sensor's performance in detecting different concentrations of sCD40L, we tested various concentrations of sCD40L (Fig. 3A). Under optimal experimental conditions, we observed a significant redshift in the wavelength as the concentration of sCD40L increased, and this redshift showed a positive correlation with the concentration. This indicates that the sensor can indirectly reflect changes in sCD40L concentration based on wavelength variation. A plot of the concentration of sCD40L *versus* the wavelength corresponding to the highest peak of the spectral curve yields the result shown in Fig. 3A. The linear regression equation is $Y = 582.6 + 0.8848 \times X$, indicating a good linear relationship ($R^2 = 0.9441$). Based on the calculation, the detection limit for sCD40L antigen detection using this 1D photonic crystal is 19.7 ng mL^{-1}. The wavelength shift is primarily due to the binding between the antigen and antibody, which alters the sensor's layered structure, shifting the photonic bandgap and changing the wavelength. During the preparation of this device, to minimize non-specific contamination, we alternately fixed polyethylene glycol (PEG) and TiO_2 onto the active area of the sensor. To test the device's response to non-target molecules in blood and assess its specificity, we conducted tests with common blood interferents—ascorbic acid (AA), uric acid (UA), and bovine serum albumin (BSA) (Fig. 3B). Although the concentrations of ascorbic acid (AA), uric acid (UA), and bovine serum albumin (BSA) in the blood differ, only the wavelength of the sensor with added sCD40L shifted to red when the interferent and sCD40L concentration were both 100 ng mL^{-1}. This experimental result indicates that the interferents have a poor binding ability with the prepared sensor recognition elements, thus demonstrating the specificity of the recognition elements in binding with sCD40L.

To further verify the clinical application of the optical sensor developed in this study, we used it to detect sCD40L in serum. Fig. 3C shows sCD40L levels in the serum of healthy individuals and ACS patients, as detected by the ELISA method. Compared to the healthy group, the sCD40L levels in the ACS patient group were significantly increased ($P < 0.05$). Fig. 3D shows the detection results of sCD40L using the optical sensor, with spectral responses in different samples (ACS patients, PBS, and

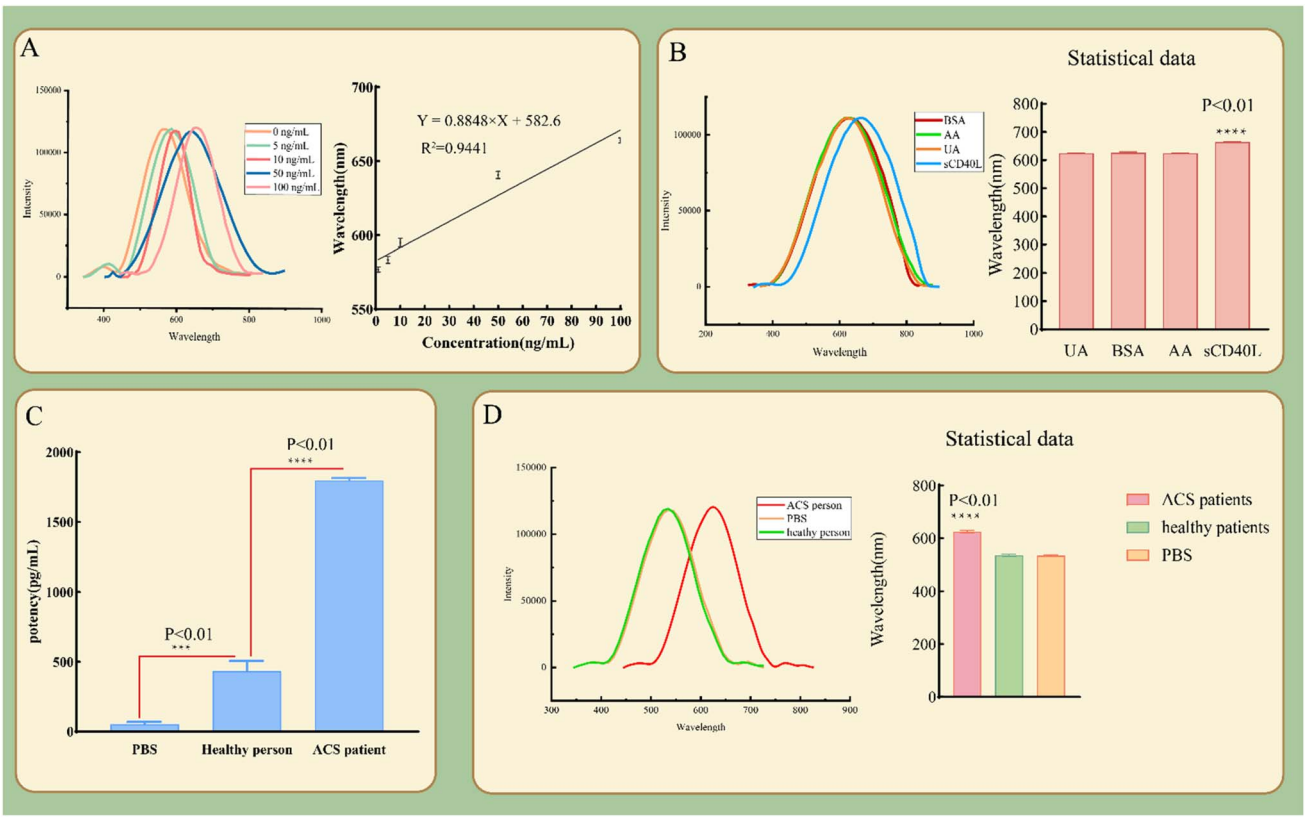

Fig. 3 Detection results of sCD40Lusing 1D photonic crystal sensors. (A) Sensitivity evaluation of the sensor for different concentrations of sCD40L. (B) Specificity evaluation of the sensor for sCD40L detection against common interferents. (C) ELISA detection results of sCD40L levels in the serum of healthy individuals and patients with ACS. (D) Detection of sCD40L in clinical serum samples using the 1D photonic crystal sensor. All data are presented as mean ± standard deviation (SD), ($n = 3$).

healthy individuals). Based on the current results, the high concentration of sCD40L in the ACS patient serum induced a strong spectral response in the sensor, while the spectral response in healthy individuals was significantly lower than that of the ACS patient group, and their wavelength did not undergo a red shift. This is consistent with the ELISA results. The above results indicate that the prepared optical sensor can effectively recognize the sCD40L levels in the serum of ACS patients and healthy individuals. sCD40L levels in the ACS patient group were significantly higher than in the healthy group, and the sensor accurately reflected this difference, demonstrating good specificity and sensitivity.

sCD40L is a type II trimeric transmembrane protein in the tumor necrosis factor (TNF) superfamily, with a molecular weight of approximately 18 kDa.[32] Studies have shown that elevated levels of sCD40L in the plasma of healthy women are associated with an increased risk of cardiovascular diseases.[33] In addition, significantly elevated levels of sCD40L can also be detected in the serum of patients with ACS. Therefore, elevated sCD40L levels are associated with an increased risk of ACS and can serve as an auxiliary diagnostic tool to help identify high-risk patients.[34] ACS patients with high sCD40L levels are at greater risk for future cardiovascular events. Detecting sCD40L in ACS patients helps assess disease prognosis. This study, based on the signal amplification effect of nanomaterials, uses the prepared nanocomposite sCD40L@SL-mTiO_2 as the recognition element to construct an optical sensor for rapid detection of sCD40L. The device can detect sCD40L because the sCD40L antibody specifically recognizes and reacts with the antigen, leading to changes in the internal structure of the sensor. This causes a shift in the position of the photonic band gap, ultimately resulting in a change in the wavelength.[35]

Unlike traditional detection devices (Table 1), this device has a simple operation process, short detection time, and low production cost. At the same time, relevant studies have shown that the photonic band gap of the visualized sensor is highly sensitive to changes in its internal structure and volume, which gives the visualized sensor very high sensitivity. Therefore, this sensor provides a new detection technology for clinical research and the diagnosis of acute coronary syndrome in cardiovascular diseases. Since sCD40L is a potential therapeutic target for cardiovascular diseases, this study provides a highly sensitive method for developing and evaluating new drugs.

3.3 Detection of organic matter decomposition performance of the sensing device

The incorporation of a composite material containing the photocatalyst TiO_2 enables photocatalytic degradation in the visible light range, thereby imparting self-cleaning capabilities to the sensor. This demonstrates the sensor's effectiveness in decomposing organic matter.[38] We selected the widely used organic dye rhodamine B as the experimental subject to conduct the organic matter decomposition experiment. To investigate the change in absorbance of rhodamine B at different concentrations under various excitation wavelengths, we used an ultraviolet-visible spectrophotometer. The absorbance of rhodamine B was measured at wavelengths ranging from 300 to 750 nm. The results showed that the maximum absorption peak of rhodamine B was at 550 nm, and as the concentration of rhodamine B decreased, the absorbance also decreased at the same excitation wavelength (Fig. 4B). This conclusion lays the foundation for the subsequent measurement of rhodamine B decomposition using 1D photonic crystals.

In the study of the organic matter decomposition performance of the 1D photonic crystal sensor, a certain concentration of rhodamine B was added to the surfaces of pure silicon wafers and 1D photonic crystal sensors, followed by ultraviolet irradiation. Samples were taken at intervals (Fig. 4C). The various components of the sensor display distinct response intensities to rhodamine B over time, reflecting their individual capabilities in recognizing and removing the pollutant. Experimental results indicate that the sensor exhibits the most pronounced decrease in response intensity during the reaction, suggesting superior adsorption or degradation efficiency and the highest sensitivity toward rhodamine B. PEG@TiO_2 shows a moderate change in response, indicating intermediate performance, whereas SiO_2 exhibits minimal variation, reflecting the weakest treatment capability. Overall, the synergistic interaction between the sensor's recognition and response units offers a clear advantage in the detection and removal of rhodamine B, highlighting its strong potential for practical application.

The TiO_2-containing sensor is capable of photocatalytically decomposing organic matter due to the unique structure of TiO_2 material (Fig. 4A). TiO_2 is a semiconductor with a bandgap whose energy matches that of ultraviolet light. When ultraviolet light is irradiated onto the surface of TiO_2, it can excite electrons in TiO_2 to transition from the valence band to the conduction band, forming free electrons and positive holes.[39] During the photonic excitation process, the generated free electrons and positive holes are high-energy reactive species that can roam on the surface of TiO_2. Some free electrons can reduce oxygen molecules in the molecules to produce active O_2^-, while the positive holes can oxidize water molecules to generate active H^+. These reactive redox species can react with organic substances,

Table 1 Comparative analysis of different sensors for detecting sCD40L

Feature/reference	Structure type	Sensitivity/response	Additional functions
rGO-TEPA/Au@BSA[36]	Electrochemical immunosensor	High	Simultaneous detection of hsCRP and sCD40L
AuNPs-*b*-PEI-*c*-MWCNT/GCE[37]	Electrochemical immunosensor	High	Reusable
PEG/TiO_2@sCD40L@SL-mTiO_2 (this work)	Photonic crystal sensor	High	Self-cleaning, antibacterial

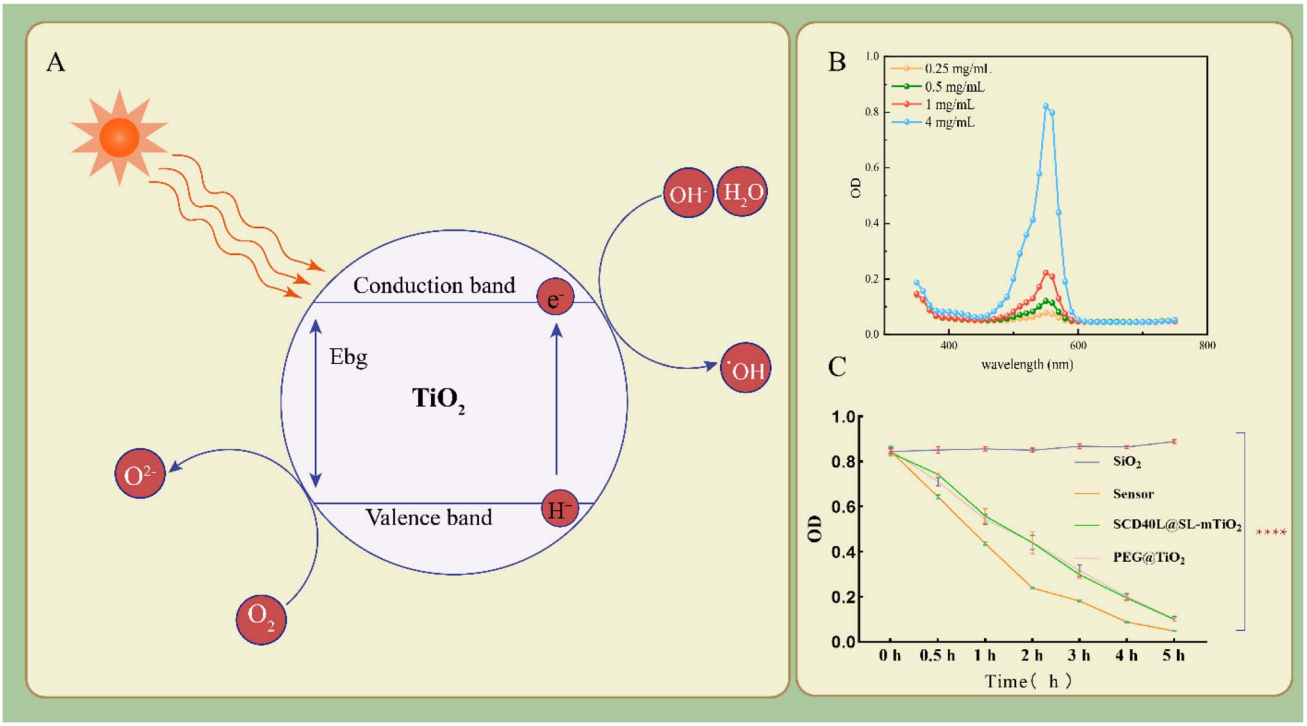

Fig. 4 Analysis of the organic matter decomposition effect of 1D photonic crystal sensors. (A) Schematic illustration of the photocatalytic degradation mechanism of organic matter by TiO_2. (B) Ultraviolet-visible absorption spectra of rhodamine B at different concentrations. (C) Photocatalytic degradation of RhB by the 1D photonic crystal sensor over time. All data are presented as mean ± standard deviation (SD), ($n = 3$), (****$P < 0.01$).

leading to the oxidation, cleavage, and degradation of the organic matter, breaking it down into small molecules or harmless products, such as water and carbon dioxide.[40] Due to the photocatalytic effect of TiO_2 under light exposure, the prepared sensor has the following advantages compared to traditional sensors: (1) The photocatalytic effect helps remove dirt attached to the surface of the sensor, achieving a self-cleaning effect, and this effect persists under continuous sunlight exposure;[41] (2) The photocatalytic effect can repair the defects on the surface of TiO_2, maintaining its stability through a self-repair mechanism under light exposure;[42] (3) Since the prepared 1D photonic crystal sensor utilizes light energy to decompose pollutants into harmless substances without requiring additional steps, it aligns with today's environmental protection concepts. Therefore, applying this self-cleaning 1D photonic crystal in disease detection will save more manpower and resources.

3.4 Analysis of the antibacterial performance of the sensor

When the sensor is exposed to air for an extended period, bacteria can easily proliferate, leading to a shortened sensor lifespan and potential environmental pollution. Therefore, it is necessary to impart certain antibacterial properties to the sensor. TiO_2 not only catalyzes the decomposition of organic matter but also demonstrates strong antibacterial activity. Previous studies have confirmed that sensors utilizing TiO_2 as a sensing element exhibit effective antibacterial performance.[43,44] Therefore, in this study, TiO_2 was incorporated into the sensing element to prepare a sensor with antibacterial properties, and the antibacterial performance of the sensor was evaluated. *E. coli* attached to the surfaces of the monocrystalline Si wafer and the sensor were collected. The samples were serially diluted, plated onto LB agar, and incubated at 37 °C for 24 hours. As shown in Fig. 5A, it is evident that the control group showed almost no bacterial colony growth, the *Escherichia coli* in the monocrystalline Si group grew vigorously in the LB medium, while the bacteria in the sensor group grew slowly. At the same time, the live/dead bacterial staining results (Fig. 5B) show that both live and dead bacteria coexist in the sensor group, while the control group and monocrystalline Si group contain mostly live bacteria with no dead bacteria present. This indicates that the prepared sensor has excellent antibacterial ability.

In addition, we studied the antibacterial capacity of the sensor using optical density (OD) measurements. As the incubation time increases, *Escherichia coli* continuously proliferates, and the optical density of the bacteria increases accordingly. Therefore, the OD600 also increases. As shown in Fig. 5C, at 0 hours, the absorbance of *Escherichia coli* in both the monocrystalline Si group and the sensor group was the same, with no statistical significance. At 12 hours, *E. coli* in the monocrystalline Si group continued to proliferate, and the OD600 value increased accordingly. In contrast, the OD600 value of *Escherichia coli* in the sensor group decreased. Statistical analysis of the two groups showed a $P < 0.05$, indicating statistical

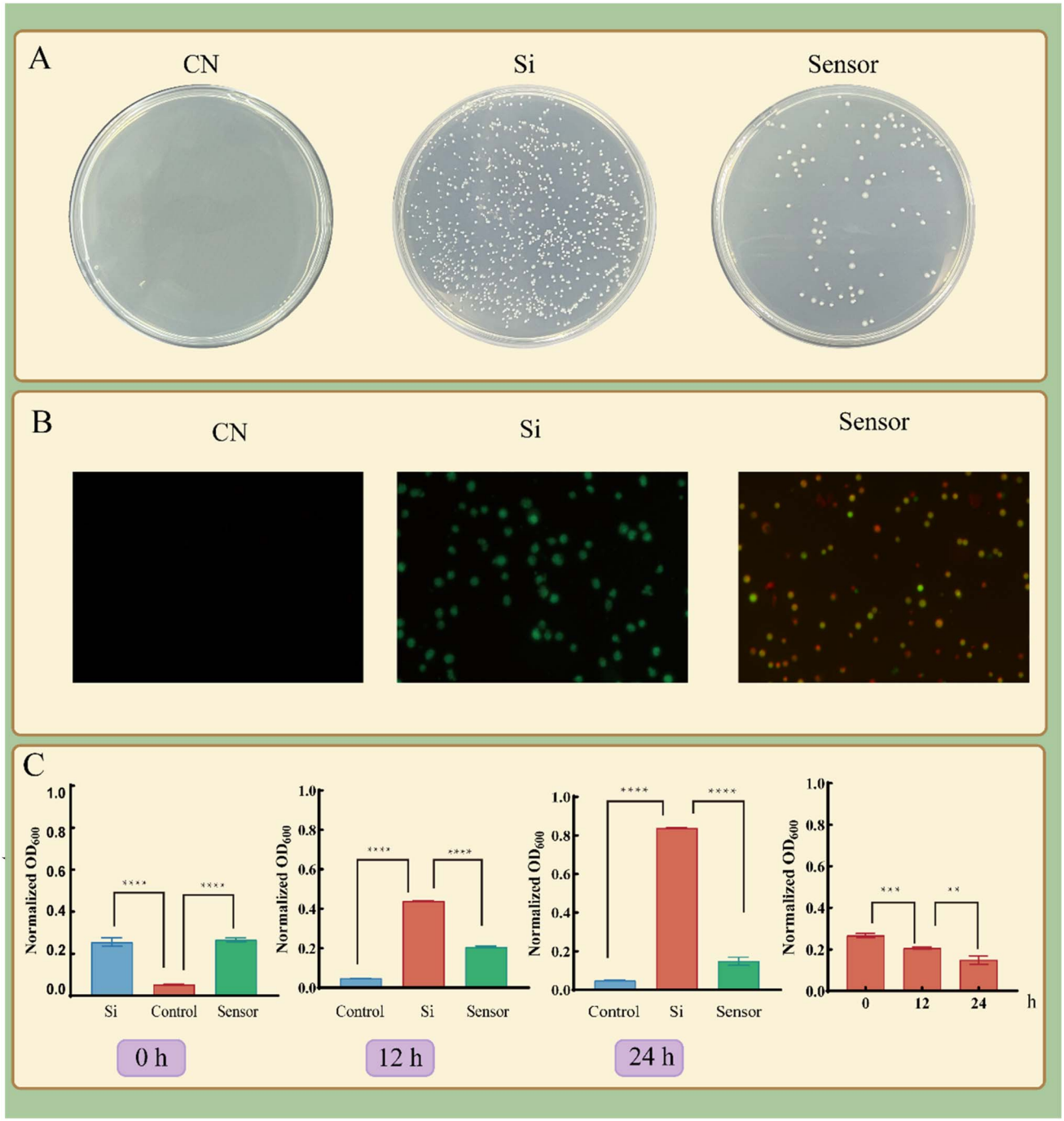

Fig. 5 Analysis of the antibacterial performance results of the 1D photonic crystal. (A) Colony formation in each group. (B) Live/dead bacterial staining results in each group. (C) OD600 measurement results of each group at different time points. Data are presented as means ± SD ($n = 3$), (**, ***, ****$P < 0.05$).

significance. This means that the prepared sensor has antibacterial properties. At 24 hours, the OD600 of *E. coli* in the monocrystalline Si group was about 0.8, while the OD600 of *E. coli* in the sensor group was only around 0.15. Additionally, we performed statistical analysis on the OD600 of *Escherichia coli* in the sensor group at different time points (0 h, 12 h, 24 h). The results showed that as time increased, the OD600 of *E. coli* also decreased. This further demonstrates that the prepared sensor has excellent antibacterial performance. Unlike traditional antibacterial materials, the antibacterial mechanism of TiO_2 is mainly reflected in the following aspects: (1) When TiO_2 is exposed to UV light, it can generate reactive oxygen species (ROS), which can damage the bacterial outer membrane, ultimately leading to bacterial injury;[45] (2) under photocatalytic action, the electronic structure of TiO_2 allows electrons to be excited from the valence band to the conduction band,

particularly under ultraviolet irradiation, while corresponding holes are generated in the valence band. These electrons and holes separate and migrate to different locations on the particle surface under the influence of an electric field, triggering a series of reactions. Oxygen molecules capture electrons to form superoxide anion radicals, while holes oxidize adsorbed OH and H_2O on the TiO_2 surface to form hydroxyl radicals (·OH), which have strong oxidative power. These radicals attack the unsaturated bonds of organic matter or acquire hydrogen atoms to generate new free radicals, initiating a chain reaction that ultimately leads to bacterial degradation;[46] (3) quantum size effect: The photogenerated electrons and holes in nanoscale titanium dioxide migrate from the bulk to the surface in a very short time, enabling them to exert a more effective antibacterial effect.[45] Therefore, after incorporating TiO_2 into the sensor, even if pathogenic microorganisms are present in the sample to be tested or in the air, they can be effectively decomposed. This not only reduces the incidence of hospital-acquired infections but also protects the safety of patients and medical staff.

4 Conclusion

In summary, this study successfully prepared nano sCD40L@SL-mTiO_2 and used it as a recognition element to construct an optical sensor for the specific detection of sCD40L. The uniqueness of this study lies in the sensor's ability to interact with incident light, exciting localized and propagating surface plasmons, thereby generating an enhanced transmission (EOT) phenomenon. By covering the surface of monocrystalline silicon with media of different refractive indices, a structure with localized surface plasmon resonance (LSPR) can be designed. This structure can significantly enhance the interaction between light and matter, thereby enabling the EOT signal in the near-infrared wavelength range. This study reports that the device exhibits high sensitivity in detecting sCD40L, capable of detecting within a broad concentration range (100 ng mL^{-1}). By using a highly specific ligand to recognize sCD40L, it shows significant selectivity toward interferents (such as uric acid, ascorbic acid, and bovine serum albumin), thereby enhancing the detection performance. This technology demonstrates excellent performance in terms of stability, reusability, and high sensitivity, making it suitable for various biological media. Therefore, this sensor provides a new detection technology for clinical research and diagnosis of acute coronary syndrome in cardiovascular diseases. At the same time, as sCD40L is a target for the treatment of cardiovascular diseases, this study provides a highly sensitive experimental method for the development and evaluation of new drugs for cardiovascular diseases.

Declarations

Ethics approval and consent to participate

All experiments were performed in accordance with the Guidelines of the Declaration of Helsinki, and experiments were approved by the Ethics Committee of the People's Hospital of Kaizhou District, Chongqing (No. 20240708). Informed consents were obtained from all human participants of this study.

Data availability

The data supporting the findings of this study are available from the corresponding author upon reasonable request.

Author contributions

Xiaoqi Li and Zhiyu Zhang were responsible for study design and manuscript writing. Liyuan Wang and Taotao Liu conducted the experiments. Heng Zhu and Lei Rong were responsible for data collection and analysis. Yun Du and Changpeng Zhai performed data visualization. Shaoshen Wang and Jie Tan participated in manuscript revision and formatting. Jing Huang was responsible for project management and research supervision.

Conflicts of interest

The authors declare that they have no conflict of interest.

Acknowledgements

This work was supported by grants from the National Natural Science Foundation of China (No. 82170445), the Major Scientific Instrument Development Project of the National Natural Science Foundation of China (No. 32127802) and the Medical technology innovation "Unveiling Command Project" of the Second Affiliated Hospital of Chongqing Medical University (No. 2023IIT094).

References

1 A. A. Damluji, D. E. Forman, T. Y. Wang, J. Chikwe, V. Kunadian, M. W. Rich, B. A. Young, R. L. Page, 2nd, H. A. DeVon and K. P. Alexander, Management of Acute Coronary Syndrome in the Older Adult Population: A Scientific Statement From the American Heart Association, *Circulation*, 2023, **147**, e32–e62.

2 B. A. Bergmark, N. Mathenge, P. A. Merlini, M. B. Lawrence-Wright and R. P. Giugliano, Acute coronary syndromes, *Lancet*, 2022, **399**, 1347–1358.

3 B. Alahmad, H. Khraishah, D. Royé, A. M. Vicedo-Cabrera, Y. Guo, S. I. Papatheodorou, S. Achilleos, F. Acquaotta, B. Armstrong, M. L. Bell, S. C. Pan, M. de Sousa Zanotti Stagliorio Coelho, V. Colistro, T. N. Dang, D. Van Dung, F. K. De' Donato, A. Entezari, Y. L. Guo, M. Hashizume, Y. Honda, E. Indermitte, C. Íñiguez, J. J. K. Jaakkola, H. Kim, E. Lavigne, W. Lee, S. Li, J. Madureira, F. Mayvaneh, H. Orru, A. Overcenco, M. S. Ragettli, N. R. I. Ryti, P. H. N. Saldiva, N. Scovronick, X. Seposo, F. Sera, S. P. Silva, M. Stafoggia, A. Tobias, E. Garshick, A. S. Bernstein, A. Zanobetti, J. Schwartz, A. Gasparrini and P. Koutrakis, Associations Between Extreme Temperatures

and Cardiovascular Cause-Specific Mortality: Results From 27 Countries, *Circulation*, 2023, **147**, 35–46.

4 R. C. Woodruff, X. Tong, S. S. Khan, N. S. Shah, S. L. Jackson, F. Loustalot and A. S. Vaughan, Trends in Cardiovascular Disease Mortality Rates and Excess Deaths, 2010-2022, *Am. J. Prev. Med.*, 2024, **66**, 582–589.

5 D. Zhang, H. Zhang, H. Sun, Y. Yang, W. Zhong, Q. Chen, Q. Ren, G. Jin and Y. Zhang, Differential identification of GSH for acute coronary syndrome using a colorimetric sensor based on nanoflower-like artificial nanozymes, *Talanta*, 2024, **266**, 124967.

6 V. Henn, S. Steinbach, K. Büchner, P. Presek and R. A. Kroczek, The inflammatory action of CD40 ligand (CD154) expressed on activated human platelets is temporally limited by coexpressed CD40, *Blood*, 2001, **98**, 1047–1054.

7 K. Jurk and B. E. Kehrel, Platelets: Physiology and Biochemistry, *Semin. Thromb. Hemostasis*, 2024, **50**, 794–803.

8 G. Pesau and G. H. Schernthaner, sCD40L: An overestimated marker for cardiovascular risk prediction?, *Atherosclerosis*, 2019, **291**, 122–123.

9 C. Chen, M. Zheng, W. Wang and W. Yu, Elevated circulating inflammatory biomarker levels in the SIRT1-NF-κB-sCD40L pathway in patients with acute myocardial infarction: a case-control study, *Ann. Med.*, 2023, **55**, 2284366.

10 F. Angeli, P. Verdecchia, S. Savonitto, S. Cavallini, A. Santucci, S. Coiro, R. Sclafani, C. Riccini, S. De Servi and C. Cavallini, Soluble CD40 ligand and outcome in patients with coronary artery disease undergoing percutaneous coronary intervention, *Clin. Chem. Lab. Med.*, 2022, **60**, 118–126.

11 I. Fernández Bello, M. T. Álvarez, F. J. López-Longo, E. G. Arias-Salgado, M. Martín, V. Jiménez-Yuste, A. Rodríguez de la Rúa and N. V. Butta, Platelet soluble CD40L and matrix metalloproteinase 9 activity are proinflammatory mediators in Behçet disease patients, *Thromb. Haemostasis*, 2012, **107**, 88–98.

12 S. Liu, H. Yang, C. Tang, Z. Yi, Y. Yi, J. Wang and B. Li, Highly sensitive photonic crystal optic fiber with annular stomatal arrangement for cervical cancer cell detection, *Phys. Lett. A*, 2025, 130574.

13 M. Hao, Z. Li, X. Huang, Y. Wang, X. Wei, X. Zou, J. Shi, Z. Huang, L. Yin, L. Gao, Y. Li, M. Holmes and H. Elrasheid Tahir, A cell-based electrochemical taste sensor for detection of Hydroxy-α-sanshool, *Food Chem.*, 2023, **418**, 135941.

14 G. Sancho-Fornes, M. Avella-Oliver, J. Carrascosa, E. Fernandez, E. M. Brun and Á. Maquieira, Disk-based one-dimensional photonic crystal slabs for label-free immunosensing, *Biosens. Bioelectron.*, 2019, **126**, 315–323.

15 S. Cheng, W. Li, H. Zhang, M. N. Akhtar, Z. Yi, Q. Zeng, C. Ma, T. Sun, P. Wu and S. Ahmad, High sensitivity five band tunable metamaterial absorption device based on block like Dirac semimetals, *Opt. Commun.*, 2024, 130816.

16 Z. Zeng, H. Liu, H. Zhang, S. Cheng, Y. Yi, Z. Yi, J. Wang and J. Zhang, Tunable ultra-sensitive four-band terahertz sensors based on Dirac semimetals, *Photonics Nanostructures: Fundam. Appl*, 2024, 101347.

17 G. Xuncen, T. Chaojun, Y. Zao, C. Shubo, W. Junqiao and L. Boxun, Design and application of multi-absorption and highly sensitive monolayer graphene microstructure absorption devices located at terahertz frequencies, *Curr. Appl. Phys*, 2025, 16–25.

18 Q. Yan, S. Li, X. Tao, T. Wang, X. Xu, X. Wang, H. Li, X. Chen and Z. Bian, Self-Cleaning and Shape-Adaptive Triboelectric Nanogenerator-Contained TiO(2) Nanoparticle Coating, *ACS Appl. Mater. Interfaces*, 2022, 49755–49764.

19 A. B. Fuertes and M. Sevilla, Hierarchical microporous/mesoporous carbon nanosheets for high-performance supercapacitors, *ACS Appl. Mater. Interfaces*, 2015, **7**, 4344–4353.

20 H. Wang, J. Xu, K. Li, Y. Dong, Z. Du and S. Wang, Highly stretchable, self-healable, and self-adhesive ionogels with efficient antibacterial performances for a highly sensitive wearable strain sensor, *J. Mater. Chem. B*, 2022, **10**, 1301–1307.

21 L. Goñi-Ciaurriz and I. Vélaz, Antibacterial and degradable properties of β-cyclodextrin-TiO(2) cellulose acetate and polylactic acid bionanocomposites for food packaging, *Int. J. Biol. Macromol.*, 2022, **216**, 347–360.

22 Q. Zhao, J. Wu, Y. Li, R. Xu, X. Zhu, Y. Jiao, R. Luo and X. Ni, Promotion of bone formation and antibacterial properties of titanium coated with porous Si/Ag-doped titanium dioxide, *Front. Bioeng. Biotechnol.*, 2022, **10**, 1001514.

23 M. R. Araujo, L. S. P. Maia, M. A. R. Miranda, Y. Martínez-Camejo, J. M. Sasaki and G. F. Guimarães, Optimization of nanoparticles for application in optical sensors, *Sens. Actuators, A*, 2023, 114923.

24 Z. Moradi, H. Fallah and M. Hajimahmoodzadeh, Nanocomposite perovskite based optical sensor with broadband absorption spectrum, *Sens. Actuators, A*, 2018, 47–51.

25 N. Shehata, E. Samir and S. Gaballah, New optical sensor for peroxides using neodymium-doped-ceria nanoparticles *via* fluorescence-quenching technique, *Sens. Actuators, B*, 2016, 341–348.

26 A. E. Schedl, I. Howell, J. J. Watkins and H. W. Schmidt, Gradient Photonic Materials Based on One-Dimensional Polymer Photonic Crystals, *Macromol. Rapid Commun.*, 2020, **41**, e2000069.

27 L. Punga, A. Abbassi, M. Toma, T. Alupului, C. Doroftei, M. Dobromir, D. Timpu, F. Doroftei, L. Hrostea, G. G. Rusu, A. Razouk and F. Iacomi, Studies of the Structure and Optical Properties of BaSrMgWO(6) Thin Films Deposited by a Spin-Coating Method, *Nanomaterials*, 2022, **12**, 2756.

28 S. Hu, H. Xu, B. Zhou, S. Xu, B. Shen, B. Dong, Z. Yin, S. Xu, L. Sun, J. Lv, J. Wang, W. Xu, X. Bai, L. Xu, S. Mintova and H. Song, Double Stopband Bilayer Photonic Crystal Based Upconversion Fluorescence PSA Sensor, *Sens. Actuators, B*, 2020, 128816.

29 A. Leonardi, Whole pair distribution function modeling: the bridging of Bragg and Debye scattering theories, *IUCrJ*, 2021, 257–269.

30 Y. Zhang, Y. Qi, R. Wang, T. Cao, W. Ma and S. Zhang, Nonintrusively Adjusting Structural Colors of Sealed Two-Dimensional Photonic Crystals: Immediate Transformation between Transparency and Intense Iridescence and Their Applications, *ACS Appl. Mater. Interfaces*, 2021, 13861–13871.

31 W. Zheng, X. Luo, Y. Zhang, C. Ye, A. Qin, Y. Cao and L. Hou, Efficient Low-Cost All-Flexible Microcavity Semitransparent Polymer Solar Cells Enabled by Polymer Flexible One-Dimensional Photonic Crystals, *ACS Appl. Mater. Interfaces*, 2020, 23190–23198.

32 E. R. Ahn, G. Lander, W. Jy, C. J. Bidot, J. J. Jimenez, L. L. Horstman and Y. S. Ahn, Differences of soluble CD40L in sera and plasma: implications on CD40L assay as a marker of thrombotic risk, *Thromb. Res.*, 2004, **114**, 143–148.

33 X. Xu, H. Huang, M. Cai, Y. Qian, Z. Li, H. Bai, Y. Han, L. Xiao, W. Zhou, X. Wang and B. Shi, Combination of IL-1 receptor antagonist, IL-20 and CD40 ligand for the prediction of acute cellular renal allograft rejection, *J. Clin. Immunol.*, 2013, **33**, 280–287.

34 T. Stadlbauer, B. Molitor, W. Jochen, P. Harwaldt, M. Schaub, H. Hoelschermann, H. Tillmanns and W. K. Hofmann, Abstract 559: Elevated Level of sCD40L During Acute Coronary Syndrome Leads to Systemic MIP-2 Release, *Circulation*, 2008, **118**, S580.

35 S. Li, Z. Wang, Y. Chen, Q. Zou, Q. Zou, L. Wang, Y. Zhu and L. Wang, Preparation of chitosan/retinoic acid @ nanocapsules/TiO_2 self-cleaning one-dimensional photonic crystals and the study of the visual detection of acute promyelocytic leukemia, *RSC Adv.*, 2023, **13**(27), 18363–18370.

36 G. Yuan, C. Yu, C. Xia, L. Gao, W. Xu, W. Li and J. He, A simultaneous electrochemical multianalyte immunoassay of high sensitivity C-reactive protein and soluble CD40 ligand based on reduced graphene oxide-tetraethylene pentamine that directly adsorb metal ions as labels, *Biosens. Bioelectron.*, 2015, **72**(10), 237–246.

37 J. Wu, J. He, Y. Zhang, Y. Zhao, Y. Niu and C. Yu, Reusable voltammetric immunosensor for sCD40L, a biomarker for the acute coronary syndrome, using a glassy carbon electrode modified with a nanocomposite consisting of gold nanoparticles, branched polyethylenimine and carboxylated multiwalled carbon nanotubes, *Microchim. Acta*, 2017, **184**(6), 1837–1845.

38 T. Liu, R. Liang and W. Qin, Anti-fouling TiO(2)-Coated Polymeric Membrane Ion-Selective Electrodes with Photocatalytic Self-Cleaning Properties, *Anal. Chem.*, 2023, **95**, 6577–6585.

39 J. Arun, S. Nachiappan, G. Rangarajan, R. P. Alagappan, K. P. Gopinath and E. Lichtfouse, Synthesis and application of titanium dioxide photocatalysis for energy, decontamination and viral disinfection: a review, *Environ. Chem. Lett.*, 2023, **21**, 339–362.

40 S. Li, Z. Wang, Y. Chen, Q. Zou, Q. Zou, L. Wang, Y. Zhu and L. Wang, Preparation of chitosan/retinoic acid @ nanocapsules/TiO(2) self-cleaning one-dimensional photonic crystals and the study of the visual detection of acute promyelocytic leukemia, *RSC Adv.*, 2023, **13**, 18363–18370.

41 K. Li, M. Li, C. Xu, Z. Du, J. Chen, F. Zou, C. Zou, S. Xu and G. Li, A TiO_2 nanotubes film with excellent antireflective and near-perfect self-cleaning performances, *J. Mater. Sci. Technol.*, 2021, **88**, 11–20.

42 E. Rezvani Ghomi, S. Nouri Khorasani, M. S. Koochaki, M. Dinari, S. Ataei, M. H. Enayati, O. Das and R. Esmaeely Neisiany, Synthesis of TiO_2 nanogel composite for highly efficient self-healing epoxy coating, *J. Adv. Res.*, 2022, **43**, 137–146.

43 B. Moongraksathum and Y.-W. Chen, Anatase TiO_2 co-doped with silver and ceria for antibacterial application, *Catal. Today*, 2017, **310**, 68–74.

44 L. Zhang, H. Bai, L. Liu and D. D. Sun, Dimension induced intrinsic physio-electrical effects of nanostructured TiO_2 on its antibacterial properties, *Chem. Eng. J.*, 2017, **334**, 1309–1315.

45 A. B. Younis, Y. Haddad, L. Kosaristanova and K. Smerkova, Titanium dioxide nanoparticles: Recent progress in antimicrobial applications, *Wiley Interdiscip. Rev.:Nanomed. Nanobiotechnol.*, 2023, **15**, e1860.

46 D. A. Serov, A. V. Gritsaeva, F. M. Yanbaev, A. V. Simakin and S. V. Gudkov, Review of Antimicrobial Properties of Titanium Dioxide Nanoparticles, *Int. J. Mol. Sci.*, 2024, **25**, 10519.